ROYAL SOCIETY OF CHEMISTRY

PAPER

Check for updates

Selective atomic layer deposition of RuOx catalysts on shape-controlled Pd nanocrystals with significantly enhanced hydrogen evolution activity†

Lei Zhang,‡[a] Zhi-Jian Zhao,‡[b] Mohammad Norouzi Banis,‡[a] Lulu Li,[b] Yang Zhao,[a] Zhongxin Song,[a] Zhiqiang Wang,[c] Tsun-Kong Sham,[c] Ruying Li,[a] Matthew Zheng,[a] Jinlong Gong [iD][b] and Xueliang Sun [iD] *[a]

The electrochemical hydrogen evolution reaction (HER) is an emerging route for producing clean hydrogen. Recently, Ru-based catalysts have exhibited good activity towards the HER, making them attractive substitutes for Pt. However, the HER performance of Ru-based catalysts still cannot reach the same level as that of commercial Pt/C in acid solution. The atomic layer deposition (ALD) technique has proved to be an effective route for the preparation of noble metal catalysts on substrates. Herein, we successfully deposited RuOx catalysts on octahedral and cubic Pd seeds through an ALD process. Interestingly, we found that RuOx was selectively deposited on Pd particles when Pd/nitrogen-doped carbon nanotubes (NCNTs) were used as the substrate. Importantly, the as-prepared Pd@RuOx/NCNT showed comparable activity with state-of-the-art commercial Pt/C catalysts for the HER. The performance exceeds all of the current Ru-based nanocatalysts for the HER in acid solution. The X-ray absorption spectroscopy and X-ray photoemission spectroscopy analyses indicated that the RuOx shell consists of metallic Ru and Ru(IV). Density functional theory calculation results indicated that the Gibbs free energy of the intermediate state H* of octahedral Pd@RuOx was much lower than that of cubic Pd@RuOx, which resulted in the superior HER activity. This paper provides an example for the rational design of efficient catalysts through a combination of shape-controlled synthesis and the ALD technique.

1. Introduction

Hydrogen is a clean fuel, making it one of the most promising energy sources for large-scale applications in the twenty-first century.[1,2] Up until now, most of the hydrogen as fuel has been produced through steam reforming of methane, which produces a large amount of CO_2 during the production process.[3] It is of great importance to develop clean routes for large-scale production of hydrogen. The electrochemical hydrogen evolution reaction (HER) is an emerging route for curbing CO_2 emissions while producing clean hydrogen.[4] Platinum is considered as the most effective electrocatalyst for the HER.[5–7]

However, its low abundance, limited supply, and rising prices have motivated researchers to look for alternate catalysts with a high performance in the HER. Recently, several studies reported the good HER performance of Ru electrocatalysts.[8–13] Peng *et al.* found that free standing two-dimensional Ru nanosheets exhibited excellent HER activities.[13] However, free standing regular Ru catalysts without some specific structures cannot exhibit a good electrocatalytic performance. On the other hand, an ideal substrate can provide a high surface area to achieve high dispersity of catalysts. Furthermore, it can even tune the crystal structure and electronic structure of catalysts.[8,9] For example, Qiao *et al.* reported that an anomalous crystalline structure of Ru on g-C_3N_4 exhibited better activity towards the HER than Pt under alkaline conditions.[8] Barman and coworkers prepared one-dimensional highly crystalline RuO_2 nanowires on carbon nitride resulting in high performance for both the HER and the oxygen evolution reaction.[9] These results indicated that the substrates played an important role for tuning the electronic structures of Ru catalysts and the reaction kinetics in the HER process. However, the HER performance of Ru-based catalysts still cannot reach the same level as that of commercial Pt/C in acid solution.[8,9,14]

[a]Department of Mechanical and Materials Engineering, The University of Western Ontario, London, ON N6A 5B9, Canada. E-mail: xsun@eng.uwo.ca
[b]Key Laboratory for Green Chemical Technology of Ministry of Education, School of Chemical Engineering and Technology, Tianjin University, Collaborative Innovation Center of Chemical Science and Engineering (Tianjin), Tianjin 300072, P.R. China
[c]Department of Chemistry, University of Western Ontario, London, ON N6A 5B7, Canada

† Electronic supplementary information (ESI) available. See DOI: 10.1039/c8ta08931k

‡ These authors contributed equally to this work.

This journal is © The Royal Society of Chemistry 2018

J. Mater. Chem. A, 2018, **6**, 24397–24406 | 24397

Currently, Pd is considered as an ideal substrate for the synthesis of core–shell Ru-based nanocrystals (NCs).[15,16] However, Ru catalysts are mainly developed based on wet-chemical reduction methods.[15–17] The surfactants involved in the reaction are difficult to remove and can hinder the catalytic activities. In recent years, application of surfactant free synthesis methods such as the atomic layer deposition (ALD) technique for the deposition of noble metal nanoparticles have gained considerable attention.[18–23] By using the ALD method, Ru catalysts can be successfully grown on several types of substrate, such as SiO_2, TiO_2 and Al_2O_3.[24,25] However, these substrates are not suitable for electrochemical catalytic reactions due to their poor electron transport. Hence, it is of great importance to select a proper substrate for the preparation of Ru-based catalysts.

As Pd has similar lattice constants to Ru, Ru atoms tend to deposit on Pd through the ALD process. In addition, the electronic structure of Ru can be controlled by tuning the morphology of the Pd particles. It can be predicted that the properties of Ru catalysts can be promoted by ALD of Ru on shape-controlled Pd nanocrystals. This paper describes a novel fabrication of Pd@RuO$_x$ core–shell catalysts on nitrogen-doped carbon nanotube (NCNT) substrates through the ALD method. RuO$_x$ was successfully deposited on both octahedral and cubic Pd seeds with two typical surface atom arrangements. Interestingly, Ru atoms were selectively deposited on Pd particles instead of NCNT substrates. The thickness of the Ru layer can be precisely controlled by tuning the ALD cycling number. The as-prepared Pd@RuO$_x$/NCNT showed comparable activity and stability with state-of-the-art commercial Pt/C catalysts for the HER in acid solution. In addition, we explored the origin of the high reaction activity of Pd@RuO$_x$/NCNT systematically by synchrotron analysis and density functional theory (DFT) calculation.

2. Results and discussion

Fig. 1a shows the main steps for the preparation of Pd@RuO$_x$ catalysts on NCNTs through the ALD method. NCNTs with a diameter range of 100 nm were prepared by ultrasonic spray pyrolysis as outlined previously.[26] First, we prepared Pd nanocubes and octahedra based on a previous method (Fig. S1†).[27] As we know, NCNTs have proved to be good support materials in fuel cell catalysts, due to their high electrochemical corrosion resistance. Hence, the Pd particles were loaded onto NCNTs before the ALD process and the loading content of Pd is 20 wt%. As shown in Fig. S2,† the particles were well dispersed on the NCNTs after ultrasonic treatment. We conducted X-ray photoelectron spectroscopy (XPS) for free standing Pd octahedra and Pd octahedra on NCNT to investigate the interaction between Pd and NCNTs (Fig. S3a–c†). When Pd octahedra were loaded on NCNTs, the Pd3d$_{3/2}$ and 3d$_{5/2}$ peaks shifted from 340.4 eV and 335.1 eV to 340.6 eV and 335.3 eV, respectively. This result indicated that after the dispersion of Pd on NCNT, the electrons transfer from Pd to NCNTs, implying a strong interaction between Pd and NCNTs. Before conducting ALD of Ru, we heated the Pd particles on NCNTs at 270 °C in the ALD chamber

for 1 h. The SEM images show that Pd octahedra maintained their morphology well during the heating process (Fig. S3d†).

ALD synthesis of Pd@RuO$_x$ bimetallic catalysts was achieved by using bis(ethylcyclopentadienyl)ruthenium(II) and oxygen (99.999%) as the precursors, and nitrogen (99.9995%) as the purge gas. The morphology of the octahedral Pd/NCNT substrates after 10, 20, 30, and 50 cycles of RuO$_x$ ALD (denoted hereafter as octahedral Pd@RuO$_x$ 10, 20, 30, and 50 ALD) was characterized using a scanning electron microscope (SEM) as shown in Fig. S4.† Although the ALD process was carried out at 270 °C, the Pd particles maintained their morphology during the whole reaction. The surface of the Pd particles on the NCNTs became rough with an increase of ALD cycling numbers. The energy-dispersive X-ray spectroscopy (EDS) results showed that the mass ratio between Ru and Pd increased from 1.3, 1.8, and 2.3, to 3.5% with increasing ALD cycles, which agrees with the results shown in SEM images.

The as-prepared octahedral Pd@RuO$_x$ 30ALD had also been characterized by transmission electron microscopy (TEM). As shown in typical low-resolution TEM and STEM images, the octahedral Pd–Ru nanocrystals were well dispersed on NCNT substrates (Fig. 1b and c). The core–shell structure of Pd@RuO$_x$ had been further clarified by high-resolution TEM (Fig. 1d and e). The thickness of the Ru layer was observed to be smaller than 5 nm. According to the HR-TEM images, the RuO$_x$ particles were successfully deposited on Pd seeds. The surfaces of the core–shell structures consisted of small Ru-based particles. The periodic fringe spaces were confirmed to be 0.31 nm, which agree well with the d values (110) of RuO$_2$. EDS line scan profiles shown in Fig. 1f and g clearly reveal the distribution of Pd and Ru elements on the whole particle. The cross-sectional compositional line-scanning profile of the individual nanocrystal showed that the onset position of the Ru signal is at around 16 nm which is 4 nm smaller than that of Pd, indicating a 4 nm thickness of the dendritic Ru shell (Fig. 1h). In addition, the EDS-mapping result shows that the Ru element existed around the Pd element, indicating that Ru is well dispersed on Pd nanoparticles (Fig. 1g). Accordingly, it can be concluded that the as-prepared nanoparticles on NCNTs were Pd@RuO$_x$ nanocrystals.

Based on the SEM and TEM observations, the surface of NCNTs was still smooth after the ALD process, indicating that no Ru atoms were deposited on the NCNT surface. We carried out a control experiment to further prove the selective deposition phenomenon. For the samples obtained by depositing Ru on Pd/NCNT substrates, the EDX spectrum showed a clear Ru signal (Fig. S5a and b†). When the Ru ALD deposition was carried out on only the NCNT substrate, the SEM images showed that no Ru particles formed on the surface. In addition, we did not observe any Ru signal in the EDX spectrum as shown in Fig. S5c and d.† As Pd and Ru have very similar radii and the lattice mismatch between Pd and fcc Ru is only 1.8% (3.89 Å $vs.$ 3.82 Å),[16] when Ru was deposited on Pd through the ALD process, the first few layers of Ru tend to exhibit an fcc structure to fit the Pd lattice. The small lattice mismatch between Pd and fcc Ru might result in the selective deposition of RuO$_x$ on Pd
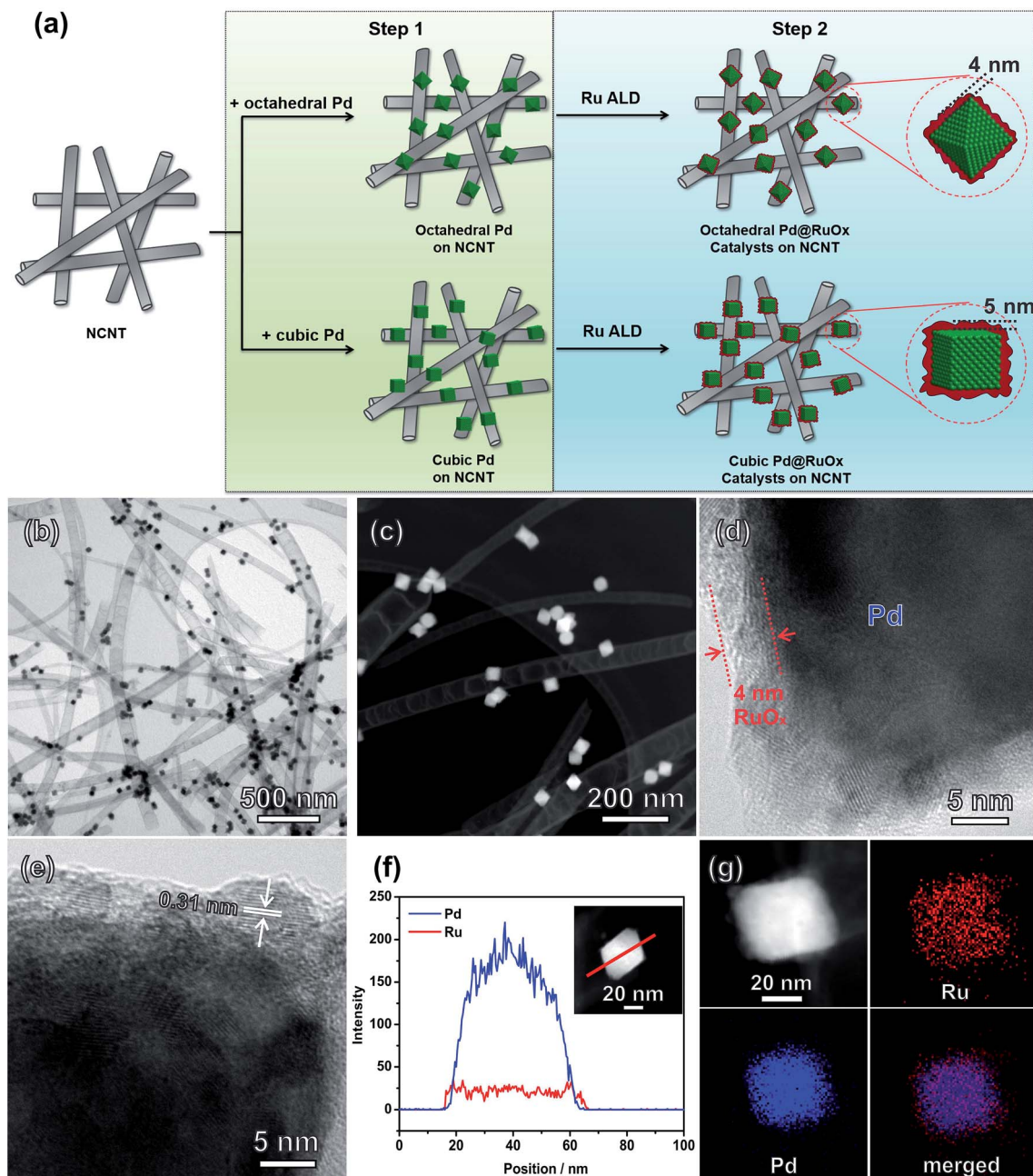
24398 | J. Mater. Chem. A, 2018, 6, 24397–24406

This journal is © The Royal Society of Chemistry 2018

Fig. 1 (a) A schematic illustration showing the formation process of the octahedral and cubic Pd@RuO$_x$ catalysts on NCNT. (b and c) The typical low-resolution TEM and STEM image of the octahedral Pd@RuO$_x$ nanocrystals. (d and e) HR-TEM images of two regions for one same nano-crystal indicating the deposition of Ru on Pd seeds. (f) HAADF-STEM-EDS cross-sectional compositional line profiles. (g) HAADF-STEM-EDS mapping image of one individual particle showing the distribution of Pd and Ru.

nanocrystals. In addition, the hydrophobic NCNTs might also cause the difficult deposition of RuO$_x$ on their surfaces.

When we were using cubic Pd seeds as substrates, Ru can also be deposited on the surface. As shown in Fig. S6,† the surface of the cubic seeds becomes rough with increasing cycling numbers. Different from the stabilization of octahedra, the cubic Pd seeds evolved to truncated morphologies due to the relatively high energy of the (100) surfaces. Similar to the octahedral Pd@RuO$_x$ on NCNT catalysts, the particles were also well dispersed on NCNTs as shown in the TEM images (Fig. 2a). The

thickness of Ru was around 5 nm. The HR-TEM images and fast Fourier transform patterns indicated the formation of a multi-crystalline structure of RuO$_2$ (Fig. 2b). Furthermore, the EDS-line scan profile and mapping data showed a clear core–shell structure formed during the ALD of Pd@RuO$_x$ of cubic Pd/NCNT (Fig. 2c–e).

The HER activity of the as-prepared octahedral and cubic Pd@RuO$_x$/NCNT after 10, 30 and 50 cycles was measured in comparison to commercial Pt/C catalysts and pure Pd nano-particles by conducting linear sweep voltammetry measurements
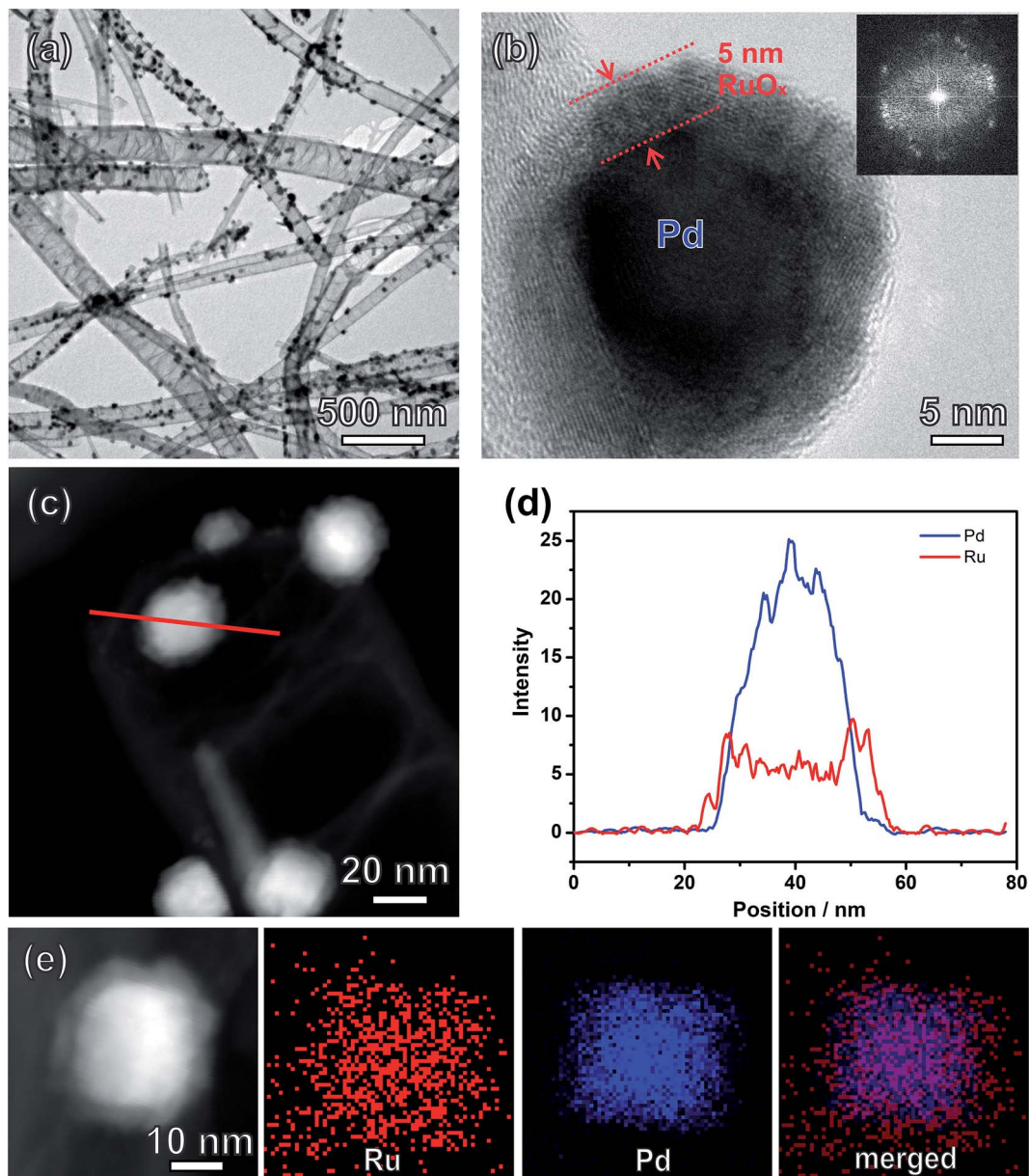
Fig. 2 (a) The typical low-resolution TEM image of the cubic Pd–RuO$_x$ nanocrystals. (b) HR-TEM image and corresponding FFT pattern of one individual particle on NCNTs. (c) STEM image of the Pd–RuO$_x$ nanocrystals on NCNTs. (d) HAADF-STEM-EDS cross-sectional compositional line profiles as marked in (c). (e) HAADF-STEM-EDS mapping image of one individual particle showing the distribution of Pd and Ru.

in 0.5 M H$_2$SO$_4$ at room temperature. The Pd particles on NCNTs exhibited a poor HER activity as shown in Fig. 3a. With the deposition of Ru on Pd seeds, the on-set potential for the HER performance shifted to the left compared to pure Pd particles. The octahedral Pd@RuO$_x$ 30ALD exhibited much better catalytic activities towards the HER compared with the octahedral Pd@RuO$_x$ 10ALD and 50ALD. More importantly, the octahedral Pd@RuO$_x$ 30ALD exhibited comparable HER activities to the commercial Pt/C catalysts (Fig. 3a). The overpotential at 10 mA cm^{-1} for the octahedral Pd@RuO$_x$ 30ALD is 33 mV, which is comparable with that of Pt/C (Fig. 3a). In addition, the performance exceeds all of the current Ru-based nanocatalysts for the HER in acid solution (Table S1†). The HER kinetics was

illustrated by the corresponding Tafel plots. Fig. 3b revealed that the Tafel slope of Pt/C catalysts was 35.6 mV dec^{-1}. Following the same measurement parameters, a similar Tafel slope was achieved for the octahedral Pd@RuO$_x$ 30ALD catalysts at 33.1 mV dec^{-1}. Empirically, the Tafel slope value within the range from 29 to 38 mV dec^{-1} can be attributed to the slow atomic combination to form H$_2$. For the cubic Pd@RuO$_x$ catalysts, the cubic Pd@Ru 30ALD also exhibited the best activity (Fig. 3c and d). The specific activity for each catalyst was calculated from the polarization curves by normalizing the current with the geometric area of the electrode. As shown in Fig. 3e, the HER activities for the octahedral Pd@RuO$_x$ 30ALD, cubic Pd@RuO$_x$ 30ALD, and Pt/C catalysts were 22.3, 8.1 and 21.9 mA cm^{-2}, respectively, at an
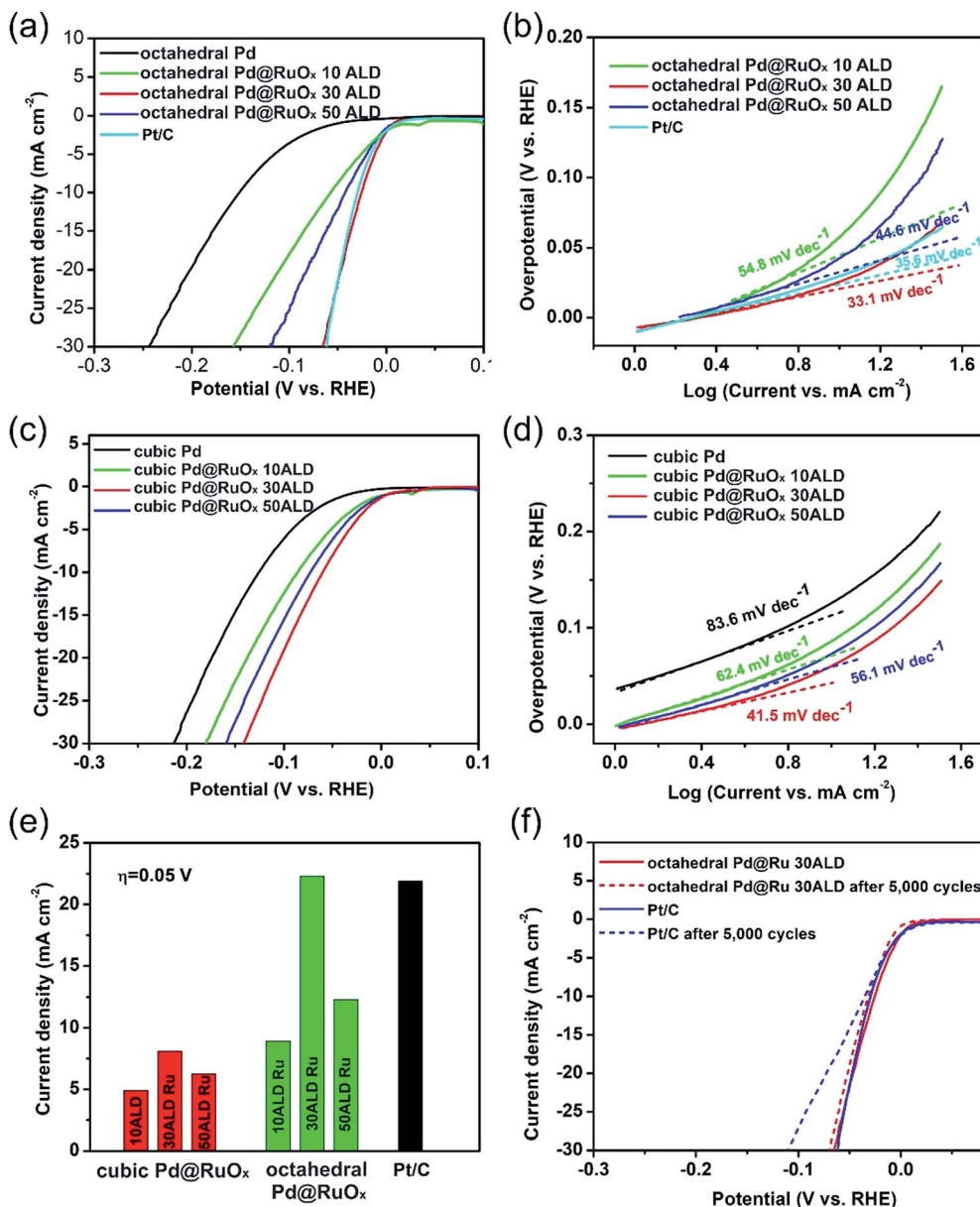
Fig. 3   (a–d) HER polarization curves and the corresponding Tafel plots recorded on octahedral and cubic Pd@RuO$_x$ nanocrystals on NCNTs with various ALD cycles, Pd octahedra and commercial Pt/C catalysts, respectively. (e) Specific current activity at 0.05 V (*versus* RHE) of the Pd–RuO$_x$/NCNT and the Pt/C catalysts for the HER. (f) Durability measurement of the Pd@RuO$_x$ 30ALD and commercial Pt/C catalysts. The polarization curves were recorded initially and after 5000 cyclic voltammetry sweeps between +0.4 and −0.15 V (*versus* RHE) at 100 mV s^{-1} in 0.5 M H$_2$SO$_4$ at a scan rate of 2 mV s^{-1}.

overpotential of 0.05 V. These findings suggest that the RuO$_x$ catalysts on Pd seeds can significantly improve the Ru performance for the HER, which can lower the cost of the catalysts. To evaluate the durability of the as-prepared Pd@RuO$_x$ catalysts, accelerated degradation tests (ADTs) were carried out between +0.4 and −0.15 V (*versus* RHE) at 100 mV s^{-1} for 5000 cyclic voltammetry sweeps. As exhibited in Fig. 3f and S7,† the octahedral Pd@RuO$_x$ 30ALD showed only a 13.1% loss in mass activity after 5000 cycles, while the loss for the Pt/C catalysts was 34.7% after 5000 cycles at an overpotential of 0.05 V. The detailed structure of the post-tested catalysts was also characterized after stability tests. As shown in Fig. S8a,† the octahedral

morphologies of Pd were maintained. The HR-TEM image (Fig. S8b†) confirmed that the periodic fringe spacing was 0.31 nm, which agrees well with the *d* values (110) of RuO$_2$. In addition, the XPS spectra after the durability test (Fig. S8c and d†) showed an obvious peak at 280.7 eV, indicating that RuO$_x$ still existed at the applied potential during HER. The above results indicated that the RuO$_x$ shell is very stable after the durability test. When RuO$_x$ was deposited on cubic or octahedral Pd nanoparticles, the ratio of Ru(0) and Ru(ɪv) was different. This means that the RuO$_x$ would create a relatively stable structure according to the surface of Pd nanocrystals. The optimized RuO$_x$ layer during the ALD process might be the reason for the good

durability during the hydrogen evolution reaction in acid solution.

To understand the effect of Pd supports on the catalytic activity of Ru catalysts and their interaction, X-ray absorption spectroscopy (XAS) was used to study the local electronic and atomic structure of the Ru catalysts (Fig. 4). A qualitative analysis of the X-ray absorption near edge structure (XANES) spectra of both samples indicated broader whiteline features compared to the Ru foil XANES spectra. This can be attributed to the smaller size of Ru clusters in the ALD samples compared to Ru Foil. Detailed examination of the white lines in the Ru K-edge XANES spectra clearly shows a shift of cubic Pd@Ru/NCNT and octahedral Pd@Ru/NCNT to higher energies compared to Ru foil. This is further illustrated in the positive shift of the edge jump of XANES spectra of both samples indicating the partial oxidation of Ru on Pd supports using the ALD process. To further illustrate the implication of Pd supports on the atomic structure of ALD Ru, the extended X-ray absorption fine structure region (EXAFS) of the Ru K-edge XAS spectra was studied in detail. The Fourier transforms of the EXAFS region for cubic Pd@Ru/NCNT, octahedral Pd@Ru/NCNT, and Ru foil are plotted in Fig. 4b. The peak at ~2.69 Å is associated with Ru–Ru atoms in the first coordination shell of metallic Ru and peaks appearing below 2 Å correspond to the bonds formed between Ru and low z elements (such as oxygen and carbon, which were not distinguishable due to the similar backscattering phase and amplitude as well as bond length). The peak intensity in these spectra is proportional to the degree of disorder/order (related to the Debye–Waller factor) and coordination number of the corresponding shell. Table 1 shows the detailed fitting parameters of the Fourier transform of the EXAFS region for both samples. In both, the EXAFS region was fit based on a mixture of Ru metal and RuO_2 crystal structures. The octahedral Pd@Ru/NCNTs had been fit with a metallic Ru–Ru total coordination number of 5.48 and RuO_2 based Ru–O coordination number of 2.56. Cubic Pd@Ru/NCNTs had a lower metallic Ru–Ru coordination number of 3.98 and RuO_2 based Ru–O coordination number of 3.17. These results can be interpreted as the formation of metallic-like Ru layers and RuO_2 layers on top of each other.

To further confirm the ratio observed between Ru(0) and Ru(IV), we investigated the surface state of the Ru@Pd catalysts by XPS (Fig. S9†). The binding energies at around 280 eV belonged to Ru 3d 5/2 spectra. The quantitative analysis of the valence distribution of Ru on the catalysts' surface was conducted based on the XPS fitted spectra. The Ru peak was fit to 3d 5/2 $RuO_2 \cdot xH_2O$, RuO_2, 3d 5/2 Sat. RuO_2 and Ru(0). By calculating the area under the fitted curve, we can conclude that the atomic ratio of metallic Ru in cubic Pd@Ru/NCNT is 25%. The metallic Ru in octahedral Pd@Ru/NCNT is greater than that in the cubic Pd@Ru/NCNT, resulting in a 32% ratio. This result also indicated that the shell consisted of Ru and RuO_2, which agrees well with the XAS data. To investigate why the octahedral Pd@RuO_x 30ALD catalyst showed higher activity for HER than the octahedral Pd@RuO_x 50ALD catalyst, we performed further characterization for the octahedral Pd@RuO_x 50ALD sample. The TEM images showed that with 50 cycles of Ru ALD, the thickness of RuO_x increased from 4 nm to 7 nm (Fig. S10a–c†). In addition, the XPS data indicated that the metallic Ru in octahedral Pd@RuO_x 50ALD was 22% (Fig. S10d†), which is much smaller than that of Pd@RuO_x 30ALD. The result indicated that an appropriate ratio of metallic Ru and Ru(IV) is critically important for the enhanced HER activity of Pd@RuO_x catalysts. The changed ratio of metallic Ru and Ru(IV) is the potential origin for the octahedral Pd@RuO_x 30ALD surpassing 50ALD.

We also performed DFT calculations to gain deeper insight into the different activities of the cubic and octahedral morphologies during the HER process. The model system was constructed based on the structural information obtained by EXAFS and XPS as discussed above (Table S2†). A number of possible structures of partially oxidized RuO_x on Pd(100) and (111) were optimized (Fig. S11†). As shown in Fig. 5a and b, the most stable configuration was used as the model to further explore the activity and mechanism of the HER process. The Gibbs free energy of the intermediate state, $|\Delta G_{H*}|$ (i.e. $|\Delta G_{HER}|$), has been considered as a major descriptor of the HER activity for a wide variety of metal catalysts. The optimum value of ΔG_{H*} should be zero. The $|\Delta G_{H*}^{Pt}|$ for the well-known highly efficient Pt catalyst that we calculated in this work is 0.11 eV,
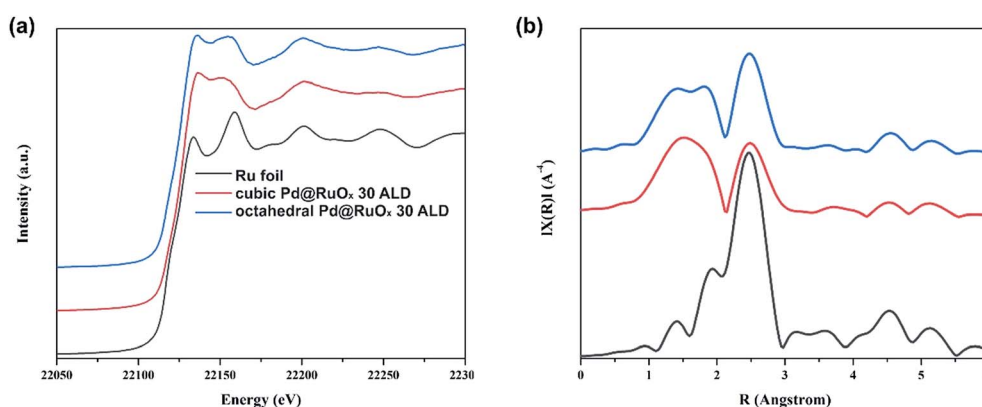

Fig. 4 (a) The normalized XANES spectra at the Ru K-edge of the cubic Pd@RuO_x 30ALD, octahedral Pd@RuO_x 30ALD and Ru foil. (b) K3 weighted Fourier transform spectra acquired from EXAFS of the cubic Pd@RuO_x 30ALD, octahedral Pd@RuO_x 30ALD, and Ru foil. The color scheme applies to all panels.

Table 1 Coordination number of Ru–Ru and Ru–O simulated from synchrotron results

Catalysts	Bonding	Coordination number	Total coordination number	Bonding distance (Å)
Octahedral Pd@Ru with 30 Ru ALD cycles	Ru–O (1)	1.06	2.56	2.032072
	Ru–O (2)	1.5		1.963143
	Ru–Ru (1)	2.74	5.48	2.63675
	Ru–Ru (2)	2.74		2.69247
Cubic Pd@Ru with 30 Ru ALD cycles	Ru–O (1)	1.26	3.17	2.026255
	Ru–O (2)	1.91		1.961154
	Ru–Ru (1)	1.99	3.98	2.62615
	Ru–Ru (2)	1.99		2.68164

which is consistent with previous literature reports that indicated a value of $|\Delta G_{H*}^{Pt}| \approx 0.09$ eV.[28] As shown in Fig. 5c and Table S3 in the ESI,† among the seven possible reaction sites of cubic Pd@RuO$_x$, the $|\Delta G_{H*}|$ on only one site is smaller than 0.11 eV ($|\Delta G_{H*}^{Pt}|$), while the other sites are not beneficial to the HER process. However in Fig. 5d, all the $|\Delta G_{H*}|$ on octahedral Pd@RuO$_x$ sites are lower than 0.11 eV which indicated that all octahedral Pd@Ru sites are highly active for the HER (Table S4†). If we define the active sites with $|\Delta G_{H*}|$ smaller than 0.11 eV, the calculated active site density of octahedral

Pd@RuO$_x$ is 9.1 nm^{-2}, which is 3 times higher than that of cubic Pd@RuO$_x$ (3.1 nm^{-2}). The calculated active site density might be the main reason for the better HER performance of the octahedral Pd@RuO$_x$ 30ALD catalysts. In addition, we constructed a metallic Ru phase single layer with corresponding structures on Pd(100) and Pd(111), and tested the H* adsorption capacity of the possible sites on the surface. As shown in the Fig. S12† and Table S5 and S6,† we found that compared with RuO$_x$, the pure metal phase Ru has a stronger adsorption free energy for H* which also indicates that the second
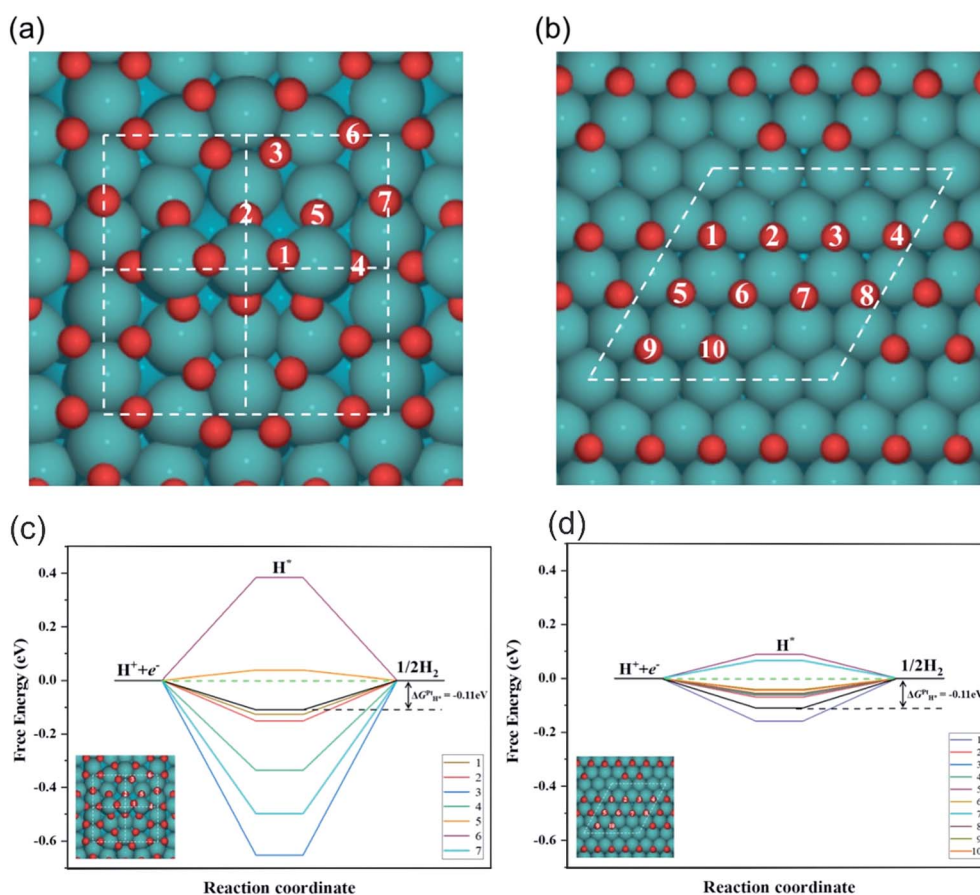

Fig. 5 (a and b) The schematic structures (top view) of different ruthenium oxide phases, Ru atoms in blue, O atoms in red. (a) RuO$_x$ (100) – white dashed line indicates the (4 × 4) unit cell with seven active sites: 1, 2, 3, 4, 5, 6, 7; (b) RuO$_x$ (111) – white dashed line indicates the (4 × 4) unit cell with ten types of active sites: 1, 2, 3, 4, 5, 6, 7, 8, 9, 10. (c and d) Free energy diagrams of possible reaction pathways for the HER on Pd@RuO$_x$ (partially oxidized) (c) (100) surface and (d) (111) surface (Ru atoms in blue, O atoms in red).

reduction process of HER requires more energy related to the surface of the RuO_x layer. Thus, comparing the overall HER performance, RuO_x consisting of Ru and RuO_2 is an active phase, which is more suitable for improved HER performance.

3. Conclusion

In summary, we successfully deposited RuO_x on octahedral and cubic Pd seeds through an atomic layer deposition (ALD) process. It was observed that when the Pd/NCNT was used as the substrate, Ru atoms were selectively deposited on Pd particles. Furthermore, the as-prepared $Pd@RuO_x$/NCNT showed comparable activity with the state-of-the-art commercial Pt/C catalysts for the hydrogen evolution reaction in acid solution. The octahedral $Pd@RuO_x$ 30ALD exhibited the best activity and good stability after 5000 cycles. The XAS and XPS spectrum indicated that the Ru shell consisted of metallic Ru and Ru(IV). DFT calculation results indicated that the Gibbs free energy of the intermediate state H* of octahedral $Pd@RuO_x$ was much lower than that of cubic $Pd@RuO_x$, which resulted in the superior HER performance. This paper provided an example for the rational design of efficient catalysts with a combination of shape-controlled synthesis and the ALD technique.

4. Experimental section

Synthesis of Pd nanocubes

105 mg of PVP ($M_w = 10\ 000$), 60 mg of AA, 600 mg of KBr, and 8 mL of DI water were mixed in a 20 mL capped vial. The mixture was pre-heated at 80 °C for 10 min in a water bath under magnetic stirring. A 3 mL solution containing 57 mg Na_2PdCl_4 was added into the pre-heated solution, after which the solution continued to mix at 80 °C for another 3 h. The samples were collected by centrifugation, washed several times with DI water, and re-dispersed in 12 mL of DI water.

Synthesis of Pd octahedra

A 3 mL solution containing 29.0 mg Na_2PdCl_4 was introduced into 8 mL of an aqueous solution containing 105 mg PVP, 100 µL HCHO, and 0.3 mL of an aqueous suspension of Pd cubic seeds. The solution was heated at 60 °C for 3 h. The samples were collected by centrifugation, washed three times with DI water, and re-dispersed in water.

ALD synthesis of RuO_x on Pd/NCNT

The Pd nanocubes and octahedra were loaded onto NCNTs by ultrasonication for 30 min. The loading amount of Pd on NCNTs was 20 wt%. Ru was deposited on the Pd particles by ALD (Savannah100, Cambridge Nanotechnology Inc., USA) using bis(ethylcyclopentadienyl)ruthenium(II) and O_2 as precursors. High-purity N_2 (99.9995%) was used as both a purge gas and carrier gas. The Pd/NCNT was loaded on aluminum foil and then put in the ALD reactor chamber. The deposition temperature was 270 °C, and the container for bis(ethylcyclopentadienyl)ruthenium(II) was kept at 110 °C to provide a steady-state flux of Ru to the reactor. Gas lines were held at

150 °C to avoid precursor condensation. For each ALD cycle, 1 s of the bis(ethylcyclopentadienyl)ruthenium(II) pulse and 5 s of the O_2 pulse were separated by a 20 s N_2 purge. The size, density and distribution of the Ru catalysts on Pd particles were precisely controlled by adjusting the number of ALD cycles.

Electrochemical measurements

The electrochemical measurements were performed using a glassy carbon rotating-disk electrode (Pine Instruments) as the working electrode with a platinum wire and a standard hydrogen electrode as the counter and reference electrodes, respectively. The catalyst dispersions were prepared by mixing 3 mg of catalyst in a 2 mL aqueous solution containing 1 mL of isopropyl alcohol and 30 µL of 5 wt% Nafion solution. Following the solution preparation, the mixture was ultrasonicated for 30 min. Next, the working electrode was prepared by transferring 10 µL of the aqueous catalyst dispersion onto the glassy carbon rotating disk electrode (0.196 cm²). The total loading amount of noble metal (Pd + Ru) was 2 µg. The loading amount of commercial Pt/C (20%) on the working electrode was also 2 µg for comparison. The working electrode was rotated at 1600 rpm to remove the H_2 gas bubbles formed at the catalyst surface.

Instrumentation

TEM , high-resolution TEM (HRTEM), high-angle annular dark-field scanning transmission electron microscopy (HAADF-STEM) and electro energy loss spectroscopy-line scan (EELS-line scan) were performed on a Tecnai G2 F20 microscope at 200 kV. Contact angle was measured on a OCA 15EC/ Dataphysics. Atomic force microscopy (AFM) was performed on a Dimension Icon. The structure of the obtained catalysts was characterized by atomic force microscopy (AFM, Dimension Icon/Bruker AXS), X-ray powder diffraction (XRD; Rigaku D/ MAX-2500, Cu Kα radiation) and X-ray photoelectron spectroscopy (XPS; EscaLab MK).

X-ray absorption spectroscopy

The Ru K-edge X-ray absorption fine structure measurements were conducted in fluorescence mode using beamline 20-BM-B at the Advanced Photon source (APS), Argonne National Laboratory, USA. The obtained XAS data was analyzed using Athena software. The extracted EXAFS data were weighted by k^3 to obtain the magnitude plots of the EXAFS spectra in radial space. The data was fitted using Artemis software.

Computational details

Periodic DFT calculations were carried out with the Vienna *ab initio* Simulation Package (VASP)[29] using the generalized gradient approximation (GGA) in form of the Bayesian error estimation functional with van der Waals corrections (BEEF-vdW).[30,31] The interaction between atomic cores and electrons were described by the projector augmented wave (PAW) method.[32] A cutoff energy of 400 eV for the plane-wave basis set and an atomic force convergence of 0.02 eV Å⁻¹ were employed.

24404 | *J. Mater. Chem. A*, 2018, **6**, 24397–24406

This journal is © The Royal Society of Chemistry 2018

A 4 × 4 cell was used for partially oxidized surfaces and Pt (111) facet, and 4 × 4 × 1 *k*-point mesh was used for the Brillouin zone integration. The slab was separated by at least 15 Å of vacuum. The top two layers of the slab were allowed to relax, while the bottom three layers were kept fixed.

The structures we constructed were based on the experimental characterization methods including XANES, XAS, EXAFS and XPS. Four layers of Pd (100) and (111) facets were built first. Based on the atomic ratio of metallic Ru from XPS and the total coordination number and bonding distance of Ru–O and Ru–Ru from synchrotron results (Table 1), a layer of partially oxidized Ru surface was added on top of the Pd surfaces and a certain amount of oxygen atoms were randomly dispersed so that the final possible structures were consistent with experimental characterization results (Table 1 and Table S2†). A number of possible structures of partially oxidized RuO_x on Pd(100) and (111) were optimized (Fig. S7 in ESI†). As shown in Fig. 5a and b, the most stable configuration was used as the model to further explore the activity and mechanism of the HER process.

In this work, we only considered the HER.

$$H^+ + e- + * \rightarrow H^+ \qquad (1)$$
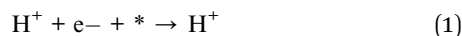
The asterisk (*) denotes the surface adsorption site. The reaction free energy of each step was calculated by the computational hydrogen electrode (CHE) model proposed by Nørskov *et al.*[33] The chemical potential of the proton–electron pair as a function of applied potential, at all pH values and temperature, can be described as

$$\mu(H^+) + \mu(e^-) = \frac{1}{2}\mu(H_{2(g)}) - eU \qquad (2)$$

Thus, at zero voltage, the free energy change of the HER can be calculated as

$$\Delta G(HER) = G(H^*) - G(slab) - [\mu(H^+) + \mu(e^-)] \qquad (3)$$

$$= G(H^*) - G(slab) - \frac{1}{2}\mu(H_{2(g)}) \qquad (4)$$

Statement of contributions

L. Zhang conceived and designed the experimental work and prepared the manuscript; M. Norouzi Banis, Y. Zhao and Z. Song helped with ALD characterization; Z. Wang and T.-K. Sham helped with XAS characterization; Z.-J. Zhao, L. Li and J. Gong performed the DFT calculations; R. Li, and M. Zheng participated in the discussion of the data; X. Sun supervised the overall project. All authors have given approval to the final version of the manuscript.

Conflicts of interest

There are no conflicts to declare.

References

1 G. W. Crabtree, M. S. Dresselhaus and M. V. Buchanan, *Phys. Today*, 2004, **57**, 39–44.
2 K. M. K. Yu, W. Tong, A. West, K. Cheung, T. Li, G. Smith, Y. Guo and S. C. E. Tsang, *Nat. Commun.*, 2012, **3**, 1230.
3 I. Chorkendorff and J. W. Niemantsverdriet, *Concepts of Modern Catalysis and Kinetics*, Wiley-VCH, 2003.
4 R. Subbaraman, D. Tripkovic, D. Strmcnik, K.-C. Chang, M. Uchimura, A. P. Paulikas, V. Stamenkovic and N. M. Markovic, *Science*, 2011, **334**, 1256–1260.
5 H. Yin, S. Zhao, K. Zhao, A. Muqsit, H. Tang, L. Chang, H. Zhao, Y. Gao and Z. Tang, *Nat. Commun.*, 2015, **6**, 6430.
6 N. Cheng, S. Stambula, D. Wang, M. N. Banis, J. Liu, A. Riese, B. Xiao, R. Li, T.-K. Sham, L.-M. Liu, G. A. Botton and X. Sun, *Nat. Commun.*, 2016, **7**, 13638.
7 J. Kye, M. Shin, B. Lim, J.-W. Jang, I. Oh and S. Hwang, *ACS Nano*, 2013, **7**, 6017–6023.
8 Y. Zheng, Y. Jiao, Y. Zhu, L. H. Li, Y. Han, Y. Chen, M. Jaroniec and S.-Z. Qiao, *J. Am. Chem. Soc.*, 2016, **138**, 16174–16181.
9 T. Bhowmik, M. K. Kundu and S. Barman, *ACS Appl. Mater. Interfaces*, 2016, **8**, 28678–28688.
10 H. Liu, G. Xia, R. Zhang, P. Jiang, J. Chen and Q. Chen, *RSC Adv.*, 2017, **7**, 3686–3694.
11 Y. Zheng, Y. Jiao, A. Vasileff and S.-Z. Qiao, *Angew. Chem., Int. Ed.*, 2018, **57**, 7568–7579.
12 X. Wang, Y. Zhu, A. Vasileff, Y. Jiao, S. Chen, L. Song, B. Zheng, Y. Zheng and S.-Z. Qiao, *ACS Energy Lett.*, 2018, **3**, 1198–1204.
13 X. Kong, K. Xu, C. Zhang, J. Dai, S. N. Oliaee, L. Li, X. Zeng, C. Wu and Z. Peng, *ACS Catal.*, 2016, **6**, 1487–1492.
14 S. Nong, W. Dong, J. Yin, B. Dong, Y. Lu, X. Yuan, X. Wang, K. Bu, M. Chen, S. Jiang, L.-M. Liu, M. Sui and F. Huang, *J. Am. Chem. Soc.*, 2018, **140**, 5719–5727.
15 J. Ge, D. He, W. Chen, H. Ju, H. Zhang, T. Chao, X. Wang, R. You, Y. Lin, Y. Wang, J. Zhu, H. Li, B. Xiao, W. Huang, Y. Wu, X. Hong and Y. Li, *J. Am. Chem. Soc.*, 2016, **138**, 13850–13853.
16 M. Zhao, L. Figueroa-Cosme, A. O. Elnabawy, M. Vara, X. Yang, L. T. Roling, M. Chi, M. Mavrikakis and Y. Xia, *Nano Lett.*, 2016, **16**, 5310–5317.
17 H. Ye, Q. Wang, M. Catalano, N. Lu, J. Vermeylen, M. J. Kim, Y. Liu, Y. Sun and X. Xia, *Nano Lett.*, 2016, **16**, 2812–2817.
18 D.-J. Lee, S.-S. Yim, K.-S. Kim, S.-H. Kim and K.-B. Kima, *Electrochem. Solid-State Lett.*, 2008, **11**, K61–K63.

This journal is © The Royal Society of Chemistry 2018

J. Mater. Chem. A, 2018, **6**, 24397–24406 | **24405**

19 H. Yan, Y. Lin, H. Wu, W. H. Zhang, Z. H. Sun, H. Cheng, W. Liu, C. L. Wang, J. J. Li, X. H. Huang, T. Yao, J. L. Yang, S. Q. Wei and J. L. Lu, *Nat. Commun.*, 2017, **8**, 1070.

20 H. Yan, H. Cheng, H. Yi, Y. Lin, T. Yao, C. L. Wang, J. L. Li, S. Q. Wei and J. L. Lu, *J. Am. Chem. Soc.*, 2015, **137**, 10484–10487.

21 S. Sun, G. Zhang, N. Gauquelin, N. Chen, J. Zhou, S. Yang, W. Chen, X. Meng, D. Geng, M. Banis, R. Li, S. Ye, S. Knights, G. Botton, T.-K. Sham and X. Sun, *Sci. Rep.*, 2013, **3**, 1775.

22 J. Liu, *ACS Catal.*, 2017, **7**, 34–59.

23 N. Cheng, Y. Shao, J. Liu and X. Sun, *Nano Energy*, 2016, **29**, 220–242.

24 S. K. Kim, J. H. Han, G. H. Kim and C. S. Hwang, *Chem. Mater.*, 2010, **22**, 2850–2856.

25 T. Aaltonen, P. Alén, M. Ritala and M. Leskelä, *Chem. Vap. Deposition*, 2003, **9**, 45–49.

26 L. G. Bulusheva, A. V. Okotrub, A. G. Kurenya, H. Zhang, H. Zhang, X. Chen and H. Song, *Carbon*, 2011, **49**, 4013–4023.

27 M. Jin, H. Liu, H. Zhang, Z. Xie and Y. Xia, *Energy Environ. Sci.*, 2012, **5**, 6352–6357.

28 J. K. Nørskov, T. Bligaard, A. Logadottir, J. R. Kitchin, J. G. Chen, S. Pandelov and U. Stimming, *J. Electrochem. Soc.*, 2005, **152**, J23–J26.

29 G. Kresse and J. Furthmüller, *Comput. Mater. Sci.*, 1996, **6**, 15–50.

30 J. Mortensen, K. Kaasbjerg, S. L. Frederiksen, J. K. Nørskov, J. P. Sethna and K. W. Jacobsen, *Phys. Rev. Lett.*, 2005, **95**, 216401.

31 J. Wellendorff, K. T. Lundgaard, A. Møgelhøj, V. Petzold, D. D. Landis, J. K. Nørskov, T. Bligaard and K. W. Jacobsen, *Phys. Rev. B: Condens. Matter Mater. Phys.*, 2012, **85**, 235149.

32 P. E. Blöchl, O. Jepsen and O. K. Andersen, *Phys. Rev. B: Condens. Matter Mater. Phys.*, 1994, **49**, 16223–16233.

33 A. A. Peterson, F. Abild-Pedersen, F. Studt, J. Rossmeisl and J. K. Nørskov, *Energy Environ. Sci.*, 2010, **3**, 1311–1315.